J|A|C|S ARTICLES

Published on Web 11/25/2009

First Observation of Phase Transformation of All Four Fe_2O_3 Phases ($\gamma \rightarrow \varepsilon \rightarrow \beta \rightarrow \alpha$-Phase)

Shunsuke Sakurai,[†,‡] Asuka Namai,[†] Kazuhito Hashimoto,[‡] and Shin-ichi Ohkoshi*[,†]

Department of Chemistry, School of Science, The University of Tokyo, 7-3-1 Hongo, Bunkyo-ku, Tokyo 113-0033, Japan, and Department of Applied Chemistry, School of Engineering, The University of Tokyo, 7-3-1 Hongo, Bunkyo-ku, Tokyo 113-8656, Japan

Received June 6, 2009; E-mail: ohkoshi@chem.s.u-tokyo.ac.jp

Abstract: Iron oxide (Fe_2O_3) has four crystal structures: γ-, ε-, β-, and α-Fe_2O_3. Until now, routes of the phase transformations among the four Fe_2O_3 phases have not been clarified because a systematic synthesis that yields all four Fe_2O_3 phases has yet to be reported. Herein we report the synthesis of a series of Fe_2O_3 nanoparticles using mesoporous SiO_2. The crystal structures of the Fe_2O_3 nanoparticles change in the order of γ-$Fe_2O_3 \rightarrow \varepsilon$-$Fe_2O_3 \rightarrow \beta$-$Fe_2O_3 \rightarrow \alpha$-$Fe_2O_3$ as the particle size increases. Threshold sizes were estimated as $\gamma \rightarrow \varepsilon$ at 8 nm, $\varepsilon \rightarrow \beta$ at 30 nm, and $\beta \rightarrow \alpha$ at 50 nm in the synthesis using $FeSO_4$ as a precursor. The phase transformations among the four Fe_2O_3 phases have been observed for the first time.

Introduction

Iron oxide (Fe_2O_3) has four crystal structures: γ-, ε-, β-, and α-Fe_2O_3.[1,2] The γ- and α-Fe_2O_3 phases have been well-studied and extensively applied in industry as magnetic (γ-Fe_2O_3) and red-dye (α-Fe_2O_3) materials.[3−9] In recent years, ε- and β-Fe_2O_3, which are rare phases, have also drawn attention. In particular, ε-Fe_2O_3 has received attention from the industrial point of view because of its large coercive field.[10−15] The crystal structures and magnetic properties of these four phases are the following: γ-Fe_2O_3 has a spinel structure (space group $Fd\bar{3}m$) and shows ferrimagnetism with a Curie temperature (T_C) of 928 K.[1,2,16,17] ε-Fe_2O_3 has an orthorhombic structure ($Pna2_1$) and exhibtis a ferrimagnetic feature (T_C = 495 K).[10−15] β-Fe_2O_3 has a bixbyite structure ($Ia\bar{3}$) and displays antiferromagnetism with a Néel temperature (T_N) of 119 K.[18−20] α-Fe_2O_3 has a corundum structure ($R3\bar{c}$) and shows a weak ferromagnetic property due to the Dzyaloshinsky−Moriya mechanism (T_C = 950 K).[21−23] From a nanomagnetic viewpoint, γ-Fe_2O_3 nanoparticles have been prepared by methods such as sol−gel techniques and electrochemical techniques.[24−26] ε-Fe_2O_3 nanoparticles have been synthesized by combining the sol−gel and reverse-micelle methods[10−12] or the sol−gel method.[13−15] β-Fe_2O_3 nanoparticles have been obtained by a chemical vapor condensation method.[27,28] Compared with γ- and α-Fe_2O_3, information about ε- and β-Fe_2O_3 is scarce. Hence, the relationship among these four phases is not so clear. To date, the phase transformations $\gamma \rightarrow \varepsilon \rightarrow \alpha$[29,30] and $\beta \rightarrow \alpha$[18−20] (depending on temperature or particle

[†] Department of Chemistry, School of Science.
[‡] Department of Applied Chemistry, School of Engineering.

(1) Zboril, R.; Mashlan, M.; Petridis, D. *Chem. Mater.* **2002**, *14*, 969.
(2) Cornell, R. M.; Schwertmann, U. *The Iron Oxides: Structure, Properties, Reactions, Occurrences and Uses*; Wiley-VCH: Weinheim, Germany, 2003.
(3) Dronskowski, R. *Adv. Funct. Mater.* **2001**, *11*, 27.
(4) Zeng, H.; Li, J.; Liu, J. P.; Wang, Z. L.; Sun, S. *Nature* **2002**, *420*, 395.
(5) Odenbach, S. *Magnetoviscous Effects in Ferrofluids*; Springer: Berlin, 2002.
(6) Lee, J. H.; Huh, Y. M.; Jun, Y. W.; Seo, J. W.; Jang, J. T.; Song, H. T.; Kim, S.; Cho, E. J.; Yoon, H. G.; Suh, J. S.; Cheon, J. *Nat. Med.* **2007**, *13*, 95.
(7) Wang, Y.; Davis, B. H. *Appl. Catal., A* **1999**, *180*, 277.
(8) Buxbaum, G.; Pfaff, G. *Industrial Inorganic Pigments*; Wiley-VCH: Weinheim, Germany, 2005.
(9) Bomatí-Miguel, O.; Mazeina, L.; Navrotsky, A.; Veintemillas-Verdaguer, S. *Chem. Mater.* **2008**, *20*, 591.
(10) Jin, J.; Ohkoshi, S.; Hashimoto, K. *Adv. Mater.* **2004**, *16*, 48.
(11) Sakurai, S.; Jin, J.; Hashimoto, K.; Ohkoshi, S. *J. Phys. Soc. Jpn.* **2005**, *74*, 1946.
(12) Ohkoshi, S.; Sakurai, S.; Jin, J.; Hashimoto, K. *J. Appl. Phys.* **2005**, *97*, 10K312.
(13) Tronc, E.; Chanéac, C.; Jolivet, J. P. *J. Solid State Chem.* **1998**, *139*, 93.
(14) Kurmoo, M.; Rehspringer, J.; Hutlova, A.; D'Orleans, C.; Vilminot, S.; Estournes, C.; Niznansky, D. *Chem. Mater.* **2005**, *17*, 1106.
(15) Gich, M.; Frontera, C.; Roig, A.; Taboada, E.; Molins, E.; Rechenberg, H. R.; Ardisson, J. D.; Macedo, W. A. A.; Ritter, C.; Hardy, V.; Sort, J.; Skumryev, V.; Nogués, J. *Chem. Mater.* **2006**, *18*, 3889.
(16) Özdemir, O. *Phys. Earth Planet. Inter.* **1990**, *65*, 125.
(17) Chikazumi, S. *Physics of Ferromagnetism*; Oxford University Press: New York, 1997.
(18) Ben-Dor, L.; Fischbein, E.; Felner, I.; Kalman, Z. *J. Electrochem. Soc.* **1977**, *124*, 451.
(19) Ikeda, Y.; Takano, M.; Bando, Y. *Bull. Inst. Chem. Res., Kyoto Univ.* **1986**, *64*, 249.
(20) Zboril, R.; Mashlan, M.; Krausova, D.; Pikal, P. *Hyperfine Interact.* **1999**, *120/121*, 497.
(21) Néel, L. *Ann. Phys.* **1949**, *4*, 249.
(22) Dzyaloshinsky, I. *J. Phys. Chem. Solids* **1958**, *4*, 241.
(23) Moriya, T. *Phys. Rev.* **1960**, *120*, 91.
(24) Willard, M. A.; Kurihara, L. K.; Carpenter, E. E.; Calvin, S.; Harris, V. G. *Int. Mater. Rev.* **2004**, *49*, 125.
(25) Jolivet, J. P.; Tronc, E.; Chanéac, C. *Eur. Phys. J. Appl. Phys.* **2000**, *10*, 167.
(26) Pascal, C.; Pascal, J. L.; Favier, F.; Moubtassim, M. L. E.; Payen, C. *Chem. Mater.* **1999**, *11*, 141.
(27) Lee, J. S.; Im, S. S.; Lee, C. W.; Yu, J. H.; Choa, Y. H.; Oh, S. T. *J. Nanoparticle Res.* **2004**, *6*, 627.
(28) Lee, C. W.; Jung, S. S.; Lee, J. S. *Mater. Lett.* **2008**, *62*, 561.
(29) Jolivet, J. P.; Tronc, W.; Chanéac, C. C. R. *Geoscience* **2006**, *338*, 488.

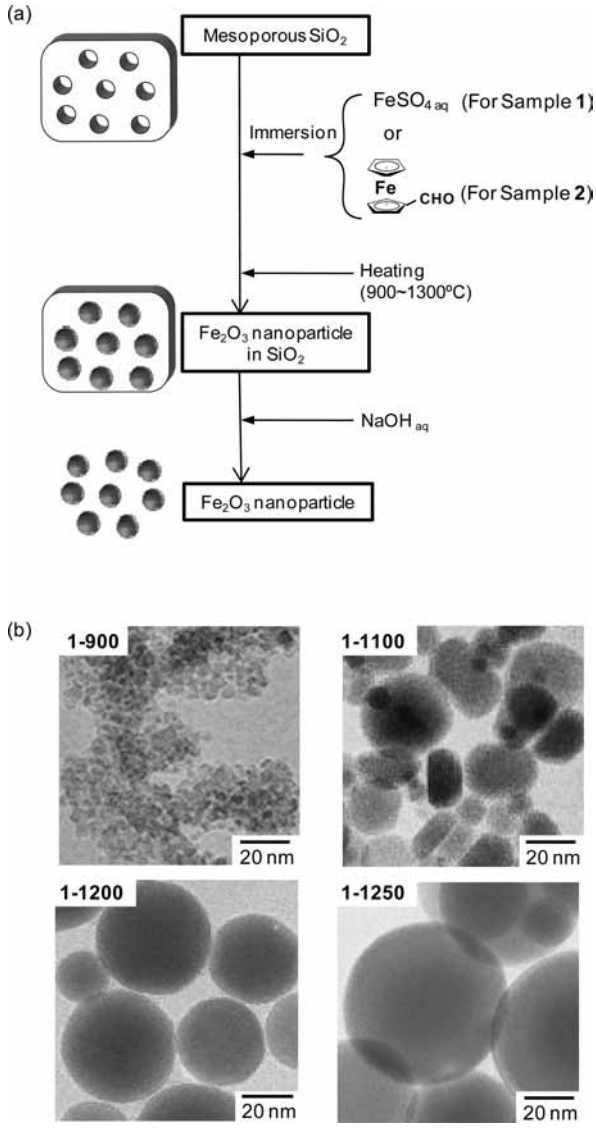

Figure 1. (a) Schematic representation of the impregnation method using mesoporous SiO_2. (b) TEM images of **1**−**900**, **1**−**1100**, **1**−**1200**, and **1**−**1250** after NaOH(aq) etching.

size) have been reported, while the following points are ambiguous: (I) Are the four phases transformed sequentially or not ? (II) If they have a sequential relationship, what is the order ? From these angles, the following sequences can possibly be considered: (i) $\gamma \rightarrow \varepsilon \rightarrow \alpha \leftarrow \beta$; (ii) $\gamma \rightarrow \beta \rightarrow \varepsilon \rightarrow \alpha$; (iii) $\beta \rightarrow \gamma \rightarrow \varepsilon \rightarrow \alpha$; and (iv) $\gamma \rightarrow \varepsilon \rightarrow \beta \rightarrow \alpha$. In the present work, we used an impregnation method with mesoporous SiO_2 to synthesize a series of Fe_2O_3 nanoparticles. With this process, we for the first time have obtained the four phases with one synthesis procedure and observed the successive sequence of the process (iv).

Experimental Section

Materials. Fe_2O_3 nanoparticles were synthesized by impregnation of an Fe compound [$FeSO_4$ or $Fe(C_{10}H_9CHO)$] into mesoporous SiO_2 particles followed by heating and etching of SiO_2 (Figure 1a). Mesoporous SiO_2 nanoparticles were synthesized using the method reported by Möller et al.[31] $Si(C_2H_5O)_4$ (62 mmol) was added to a solution composed of H_2O (4 mol), C_2H_5OH (0.18 mol), $C_{16}H_{33}N(CH_3)_3Cl$ (16 mmol), and $N(CH_2CH_2OH)_3$ (62 mmol) at 60 °C and stirred for 2 h. Mesoporous SiO_2 nanoparticles were obtained after centrifuging and heating at 600 °C in air.

Synthesis Using $FeSO_4$. The first series of Fe_2O_3 nanoparticles (**1**) was synthesized as follows. Mesoporous SiO_2 nanoparticles were immersed in a mixed solution of CH_3OH and H_2O containing $FeSO_4$ by grinding in an agate mortar and drying at 60 °C under a vacuum. The Fe/Si molar ratio was 0.08. Next, Fe_2O_3 nanoparticles embedded in a SiO_2 matrix were obtained upon heating. The as-dried materials were heated in air to 900−1250 °C at a rate of 4 °C/min. They were kept at the same temperature for 4 h and then cooled to room temperature at a rate of 5 °C/min. Finally, a series of Fe_2O_3 nanoparticle samples was obtained after etching of the SiO_2 with a 5 mol dm^{-3} NaOH aqueous solution for 24 h at 60 °C. Hereafter, these samples are called **1-*X***, where ***X*** represents the calcination temperature.

Synthesis Using $Fe(C_{10}H_9CHO)$. The second series of Fe_2O_3 nanoparticles (**2**) was synthesized as follows. Mesoporous SiO_2 nanoparticles were immersed in a mixed solution of CH_3OH and furfuryl alcohol ($C_5H_6O_2$) containing ferrocenecarbaldehyde [$Fe(C_{10}H_9CHO)$] by grinding in an agate mortar. The Fe/Si molar ratio was 0.11. Next, the Fe_2O_3 nanoparticles embedded in a SiO_2 matrix were obtained upon heating to 1000−1300 °C for 4 h. Hereafter, these samples are called **2-*X***.

Characterization. The transmission electron microscopy (TEM) images were measured with a JEOL JEM 2000EXII transmission electron microscope. The crystal structures of the obtained materials were characterized by X-ray diffraction (XRD) using a Rigaku RINT 2100 diffractometer. Rietveld analyses of the XRD patterns for all of the samples were conducted using the RIETAN-FP program.[32] The magnetic properties were measured with a superconducting quantum-interference device magnetometer (Quantum Design MPMS 7).

Results and Discussion

1-*X* Series. Figure 1b shows TEM images for the samples **1**-**900**, **1**-**1100**, **1**-**1200**, and **1**-**1250**. The TEM image of **1**-**900** shows spherical particles with an average size of 4 ± 1 nm. As the heating temperature was increased, the particles became larger: 19 ± 6 nm (**1**-**1100**), 34 ± 13 nm (**1**-**1200**), and 45 ± 18 nm (**1**-**1250**). TEM images of the other **1-*X*** samples are shown in Figure S1 in the Supporting Information (SI). The small particle size of **1**-**900** can be explained by the size of the mesopores in SiO_2 (~3 nm).[31] Below the glass transition temperature (T_g) of SiO_2 (~1000 °C),[33] SiO_2 prevents Fe_2O_3 nanoparticles from aggregating. In contrast, above T_g, the particle size grows by aggregation of Fe_2O_3 nanocrystals as a result of the softness of the SiO_2 matrix.

Figure 2a and Figure S2 in the SI show XRD patterns and Rietveld analyses of the samples. The **1**-**900** sample exhibited broad peaks, and the pattern is attributed to the γ-Fe_2O_3 phase. The broadened peaks are consistent with the small-sized γ-Fe_2O_3 nanoparticles. The pattern of **1**-**1100** showed diffraction peaks from the pure ε-Fe_2O_3 phase. The pattern of **1**-**1200** mainly consisted of the β-Fe_2O_3 phase (87%) but also contained ε-Fe_2O_3 (9%) and α-Fe_2O_3 (4%). The XRD pattern of **1**-**1250** consisted of the α-Fe_2O_3 (69%) and β-Fe_2O_3 (31%) phases. These results indicate that the crystal structures of Fe_2O_3 nanoparticles change in the order of γ-$Fe_2O_3 \rightarrow \varepsilon$-$Fe_2O_3 \rightarrow \beta$-$Fe_2O_3 \rightarrow \alpha$-$Fe_2O_3$ as the heating temperature and particle size increase (Figure 2b,c).

(30) Sakurai, S.; Tomita, K.; Hashimoto, K.; Yashiro, H.; Ohkoshi, S. *J. Phys. Chem. C* **2008**, *112*, 20212.
(31) Möller, K.; Kobler, J.; Bein, T. *Adv. Funct. Mater.* **2007**, *17*, 605.
(32) Izumi, F.; Momma, K. *Solid State Phenom.* **2007**, *130*, 15.
(33) Sakka, S.; Mackenzie, J. D. *J. Non-Cryst. Solids* **1971**, *6*, 145.

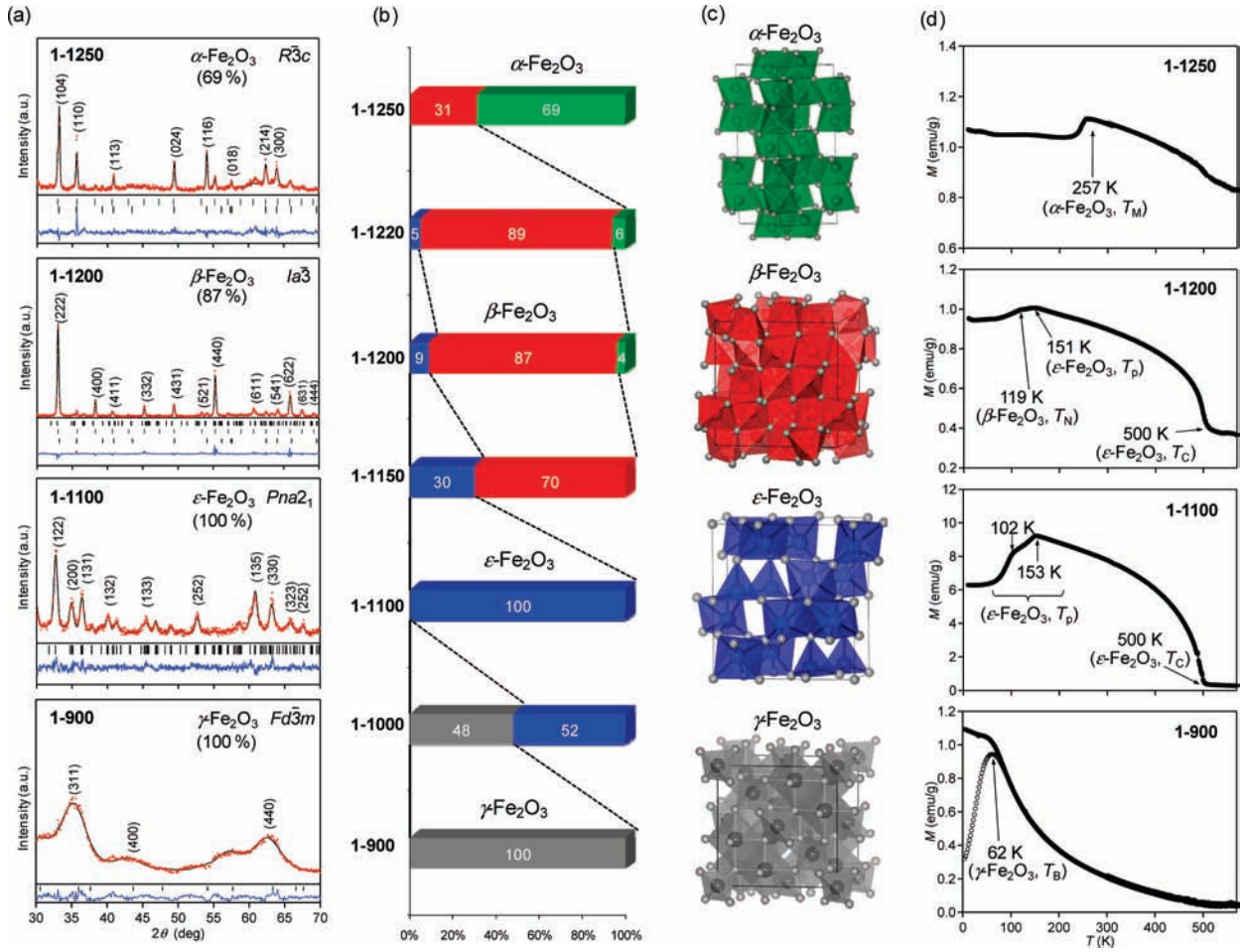

Figure 2. (a) XRD patterns and Rietveld analyses for **1-900**, **1-1100**, **1-1200**, and **1-1250**. Miller indices correspond to the unit cells of γ-Fe_2O_3, ε-Fe_2O_3, β-Fe_2O_3, and α-Fe_2O_3, respectively. (b) The contents of four Fe_2O_3 phases evaluated by Rietveld analyses. (c) Graphical representations of the crystal structures of γ-Fe_2O_3, ε-Fe_2O_3, β-Fe_2O_3, and α-Fe_2O_3. The colored spheres at the centers of polyhedrons and white spheres on the edges represent the iron and oxygen atoms, respectively. (d) Magnetization-vs-temperature curves. Black lines were measured with cooling, except for the white circles for **1-900**, which were measured with a warming process. The applied fields were 0.1 kOe for **1-900**, 1 kOe for **1-1100**, and 10 kOe for **1-1200** and **1-1250**.

Figure 2d depicts the magnetization (M)-versus-temperature (T) curves. The γ-Fe_2O_3 sample **1-900** displayed superparamagnetism with a blocking temperature (T_B) of 62 K, which is likely due to the small size of the nanoparticles. The **1-1100** sample composed of ε-Fe_2O_3 showed spontaneous magnetization with $T_C = 500$ K, but the M value decreased below 153 and 102 K because of spin reorientation (T_p). The **1-1200** sample exhibited peaks in M at 151 and 119 K; the former of these corresponds to the spin reorientation of ε-Fe_2O_3 and the latter to the antiferromagnetic phase transition at T_N of β-Fe_2O_3. The M value of **1-1250** decreased below 257 K, which corresponds to the Morin transition (T_M) of α-Fe_2O_3.[35] The magnetization (M)-versus-external magnetic field (H) plots for these samples also reflect the crystal phases (Figure S3 in the SI).

The threshold sizes of the $\gamma \rightarrow \varepsilon$, $\varepsilon \rightarrow \beta$, and $\beta \rightarrow \alpha$ phase transformations can be estimated from the relationship between the existence ratio of each phase obtained from XRD and the size distribution obtained from TEM images. Since the XRD data clearly showed the order to be $\gamma \rightarrow \varepsilon \rightarrow \beta \rightarrow \alpha$ with increasing particle size, the histogram of the particle size distribution is divided by the existence ratio of each phase, considering the volume of each particle size. For example, the existence ratio of ε-Fe_2O_3, $R(\varepsilon)$, is expressed as follows:

$$R(\varepsilon) = \frac{\sum_{d=d_{\gamma\rightarrow\varepsilon}}^{d_{\varepsilon\rightarrow\beta}} N(d)d^3}{\sum_{d=0}^{\infty} N(d)d^3}$$

where $N(d)$ is the number of particles of size of d and $d_{\gamma\rightarrow\varepsilon}$ and $d_{\varepsilon\rightarrow\beta}$ are the size thresholds for the $\gamma \rightarrow \varepsilon$ and $\varepsilon \rightarrow \beta$ phase transformations, respectively. From this relation, the threshold sizes for the Fe_2O_3 phases were estimated to have the following values: $d_{\gamma\rightarrow\varepsilon} = 8$ nm, $d_{\varepsilon\rightarrow\beta} = 30$ nm, and $d_{\beta\rightarrow\alpha} = 50$ nm,[34] as shown in Figure 3.

2-*X* Series. We examined the synthesis using $Fe(C_{10}H_9CHO)$ as a different precursor. Also in this case, the series of phase transformations $\gamma \rightarrow \varepsilon \rightarrow \beta \rightarrow \alpha$-$Fe_2O_3$ was observed (Figure 4). The TEM image of **2-1000** showed spherical particles with an average size of 4 ± 1 nm (Figure S4 in the SI). As the heating temperature increased, the particles became larger:

(34) It is noted that these threshold sizes were only for the Fe_2O_3 nanoparticle synthesized in mesoporous silica. Such particle sizes depend on the circumstances, i.e., the interface energy depends on the materials.

(35) Morin, F. J. *Phys. Rev.* **1950**, *78*, 819.

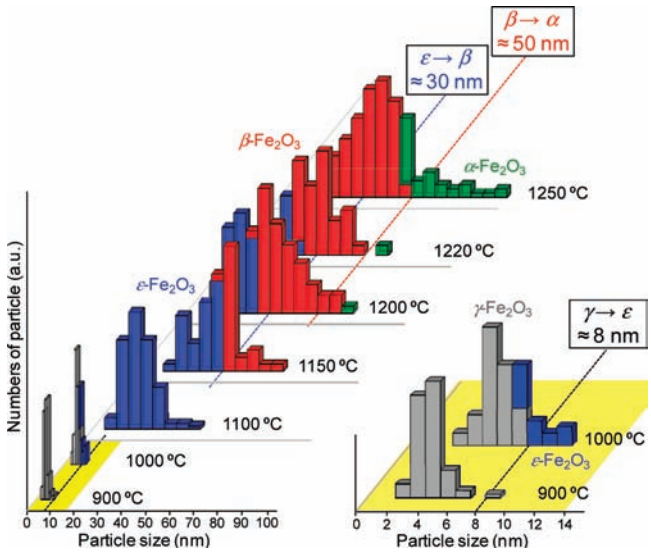

Figure 3. Particle size distributions of Fe_2O_3 nanoparticles in the series of samples **1**. The colors of the bars indicate the corresponding estimated Fe_2O_3 crystal structures: γ, gray; ε, blue; β, red; α, green. The size range of each Fe_2O_3 phase in each sample was estimated from the existence ratio of each phase from the XRD analyses. Dotted lines indicate the threshold sizes for the phase transformations among the Fe_2O_3 phases.

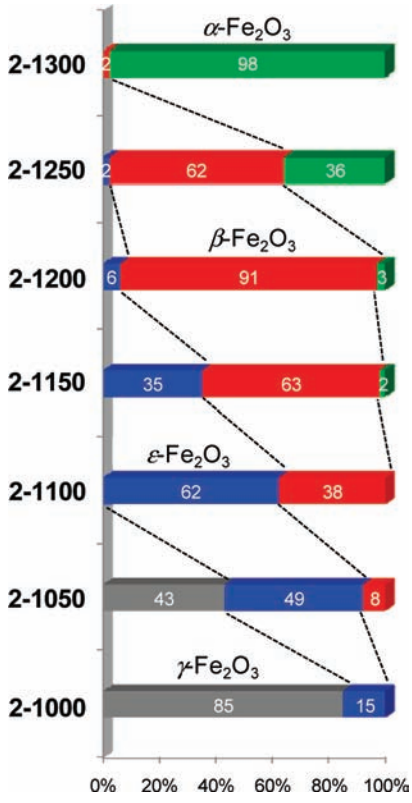

Figure 4. Contents of the four Fe_2O_3 phases calculated by Rietveld analyses for the samples obtained using $Fe(C_{10}H_9CHO)$ as the precursor (**2-*X***, ***X*** = **1000**−**1300**).

24 ± 14 nm (**2-1150**), 52 ± 22 nm (**2-1250**), and 135 ± 84 nm (**2-1300**). The XRD results indicated that the crystal structures of Fe_2O_3 nanoparticles change in the order γ-Fe_2O_3 → ε-Fe_2O_3 → β-Fe_2O_3 → α-Fe_2O_3 as the heating temperature and particle size increase (Figure S5 in the SI). The threshold sizes of the phase transformations were estimated to have the following values: $\gamma \rightarrow \varepsilon$ at 7 nm, $\varepsilon \rightarrow \beta$ at 35 nm, and $\beta \rightarrow$ α at 80 nm. The magnetic properties of the sample series **2** are almost the same as those for series **1** (Figure S6 in the SI).

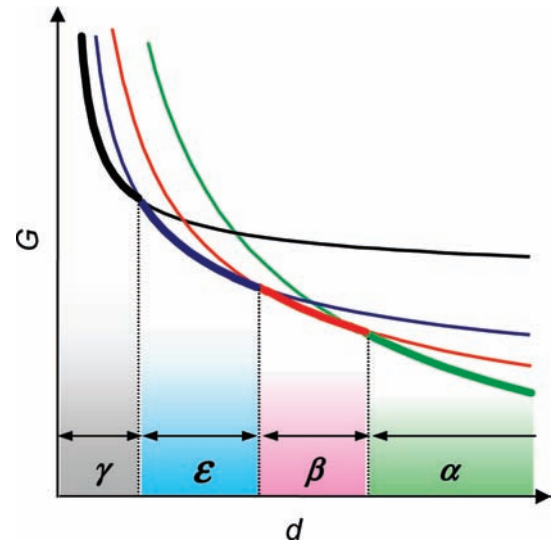

Figure 5. Representation of G vs d curves for the four Fe_2O_3 phases under the conditions $G_B(\gamma) > G_B(\varepsilon) > G_B(\beta) > G_B(\alpha)$ and $G_S(\gamma) < G_S(\varepsilon) < G_S(\beta) < G_S(\alpha)$. Gray, blue, green, and red lines represent the G values of γ-, ε-, β-, and α-Fe_2O_3, respectively. Thick solid lines indicate the most stable Fe_2O_3 phases over the corresponding size ranges.

Thermodynamic Interpretation. The phase transformations among the four Fe_2O_3 phases ($\gamma \rightarrow \varepsilon \rightarrow \beta \rightarrow \alpha$) were observed for the first time in the present study, although the phase transformations between two Fe_2O_3 phases ($\beta \rightarrow \alpha$)[18−20] and among three Fe_2O_3 phases ($\gamma \rightarrow \varepsilon \rightarrow \alpha$) were reported previously.[29,30] The observed phase transformations for the four Fe_2O_3 phases, $\gamma \rightarrow \varepsilon \rightarrow \beta \rightarrow \alpha$, are due to the surface (or interface) energy contribution to the free energy for nanoparticles inside of the mesoporous silica. The free energy of a nanoparticle is $G(i) = G_B(i) + (6V_m/d)G_S(i)$, where G_B is the free energy in the bulk, G_S is the surface energy, V_m is the molar volume, d is the diameter of the nanoparticle, and i represents the type of phase.[9,36−38] When the G_B and G_S values for the four Fe_2O_3 phases satisfy the conditions (i) $G_B(\gamma) > G_B(\varepsilon) > G_B(\beta) > G_B(\alpha)$ and (ii) $G_S(\gamma) < G_S(\varepsilon) < G_S(\beta) < G_S(\alpha)$, the G-versus-d curves should appear as shown in Figure 5. This figure indicates that the $\gamma \rightarrow \varepsilon \rightarrow \beta \rightarrow \alpha$ phase transformation can be explained by the increasing d value. As for the formation of γ-Fe_2O_3 of the initial phase, divalent iron ion is known to help the formation of γ-Fe_2O_3,[29] and hence, a divalent iron ion may contribute to the generation of the γ-Fe_2O_3 nanoparticles.

Conclusion

The present study has presented the first systematic synthesis to produce all four Fe_2O_3 phases (γ-, ε-, β-, and α-Fe_2O_3) and reported that the particle size determines the stable phase. The threshold sizes between these phases in spherical Fe_2O_3 nanoparticles prepared from $FeSO_4$ precursor are as follows: $\gamma \rightarrow \varepsilon$, 8 nm; $\varepsilon \rightarrow \beta$, 30 nm; $\beta \rightarrow \alpha$, 50 nm.

(36) McHale, J. M.; Auroux, A.; Perrotta, A. J.; Navrotsky, A. *Science* **1997**, *277*, 788.
(37) Wen, H. L.; Chen, Y. Y.; Yen, F. S.; Huang, C. H. *Nanostruct. Mater.* **1999**, *11*, 89.
(38) Zhang, H.; Banfield, J. F. *J. Mater. Chem.* **1998**, *8*, 2073.

Acknowledgment. The present research was supported in part by a Grant-in-Aid for Young Scientists (S) from JSPS, a grant for the Global COE Program "Chemistry Innovation through Cooperation of Science and Engineering", the Photon Frontier Network Program from the Ministry of Education, Culture, Sports, Science and Technology (MEXT) of Japan, the Okawa Foundation, and Shorai Foundation for Science and Technology. A part of the present research was conducted at the Center for Nano Lithography & Analysis of the University of Tokyo, supported by MEXT of Japan.

Supporting Information Available: TEM images, XRD patterns, and magnetic properties of Fe_2O_3 nanoparticles. This material is available free of charge via the Internet at http://pubs.acs.org.

JA9046069